# Heat fluxes over weak SST heterogeneity

L. Mahrt[1] and D. Khelif[2]

[1]   The spatial variability of turbulence and surface heat flux are examined for the case of small air-surface temperature difference and modest sea-surface temperature variability. As a result of nonlinearities in the bulk formula, the heterogeneity is predicted to shift the area-averaged heat flux toward more significant upward values compared to that computed from the usual bulk formula and the area-averaged air-surface temperature difference. This prediction is supported by a case study analysis of aircraft data collected over heterogeneity of the sea-surface temperature. Traditional approaches for computing the surface flux are found to be unreliable over surface heterogeneity where the scales of the transport vary horizontally. A method based on a multiresolution wavelet transform reveals the spatial variability of the flux for different scales. This information together with several additional scale-dependent indices are used to select the range of scales included in the flux computation. This approach provides more reliable estimates of the spatial variation of the flux, although uncertainties remain. Required improvements in observation strategies are discussed for quantitative evaluation of the bulk formula in conditions of surface heterogeneity.

## 1.   Introduction

[2]   A number of studies have examined the flow across large horizontal variations of SST [*Friehe et al.*, 1991; *Ullman and Cornillon,* 2000; *Thum et al.*, 2002; *Mahrt et al.*, 2004; *Pyatt et al.*, 2005; *O'Neill et al.*, 2005; *Vickers and Mahrt*, 2006; *Small et al.*, 2008]. SST is the sea-surface temperature often measured with a downward pointing radiometer. Little attention has been given to weak, smaller-scale, SST changes that can cause substantial relative variations of the turbulence in the presence of small spatially averaged air-sea temperature difference. These weaker surface temperature variations and small air-sea temperature difference occupy much of the oceanic surface in contrast to strong SST changes. Even small variations of SST can lead to significant horizontal variation of the turbulence and fluxes because the transfer coefficients are sensitive to stability for near neutral conditions. Since the surface stress is generally less over the sea compared to over land, relatively small deviations of the heat flux from zero correspond to significant changes of $z/L$ where $L$ is the Obukhov length. The impact of SST variations is greater with weaker surface stress. The transfer of heat for weakly conditions may be much larger than predicted by Monin-Obukhov similarity theory [*Smedman et al.*, 2007a]. *Smedman et al.* [2007b] attributed this behavior to possible nonstationary transitions to longitudinal rolls and unsteady detached eddies. The quantitative dependence of the heat flux on surface temperature and stability may be sensitive to time and space averaging of the input variables [*Gulev*, 1997].

[3]   The evolution of SST gradients is the net result of complex interactions between a number of processes, including the important impact of diurnal variation of radiative forcing under weak wind conditions [e.g., *Katsaros and Soloviev*, 2004; *Katsaros et al.*, 2005; *Soloviev and Lukas*, 2006]. Such time dependence of the SST field often involve interactions with the surface stress and mixing within the upper ocean. The response of the heat flux to the SST distribution is coupled to spatial variation of the surface stress, which reflects a complex integration of influences from the wind shear, wind-driven waves and swell [*Rieder and Smith*, 1998; *Grachev et al.*, 2003]. In cases where the wind is sufficiently weak compared to the swell propagation speed, the momentum flux may be weak or even upward from the swell to the atmosphere [*Smedman et al.*, 1994; *Grachev and Fairall*, 2001]. These variations of the surface stress not only influence the evolution of the SST distribution, but also influence the response of the heat flux to a given SST field.

[4]   The current case study examines the impact of modest variation of SST on the heat flux for weakly unstable conditions without attempting to unravel the above coupling mechanisms. This analysis is physically motivated by first analytically examining the behavior of spatially averaged fluxes using the bulk formula over heterogeneous surface temperature (next section).

[5]   Current approaches for computing weak fluxes in heterogeneous conditions are generally inadequate in that con-

[1]COAS, Oregon State University, Corvallis, Oregon, USA.
[2]Department of Mechanical and Aerospace Engineering, University of California, Irvine, California, USA.

siderable care is required to select the range of scales included in the flux calculation, which is one of the goals of this study. The present study develops a technique for computing fluxes over surface heterogeneity (section 4.2) that is more flexible than existing approaches based on fixed averaging lengths. This method is applied to a case study based on aircraft data over modest variation of SST (section 5).

## 2.  Illustration of the Heterogeneity Problem

[6] The bulk formula assumes that the heat flux is in equilibrium with the local air-surface temperature difference, which becomes a tentative assumption with significant SST variability. Even with equilibrium maintained over horizontal variations of the SST, the relationship of the spatially averaged heat flux to the spatially averaged air-sea temperature difference may be quite different from that predicted by the bulk formula. An extensive literature survey and examination of different contributions to these differences are presented by *Gulev* [1997] for different scenarios of time and space averaging.

[7] In the following plausibility exercise, the influence of the SST heterogeneity on a generic variable, $\phi$, is posed in terms of a regional average, $[\phi]$, and the deviation of a local mean from the regional average, $\phi^*$. The turbulence quantities, $\phi'$, are deviations from the local mean. For examination of horizontal variation of surface fluxes, the horizontal scale for the calculation of the local mean must be large enough to include an adequate sample of the transporting eddies, but small enough to resolve as much of the horizontal heterogeneity as possible.

[8] The turbulence kinematic heat flux averaged over the region (flight track) can be expressed in terms of the usual bulk formulation as

$$[w'\theta'] = -C_h V[\Delta T].  \qquad (1)$$

where the horizontal brackets indicates a regional average, $C_h$ is the transfer coefficient for heat and $V$ is the speed of the vector-averaged wind speed. $\Delta T$ is the air-sea potential temperature difference, defined as

$$\Delta T \equiv \theta - T_{sfc},  \qquad (2)$$

where $T_{sfc}$ is the surface temperature, $\theta$ is the local potential temperature

$$\theta \equiv T + 0.01 Km^{-1}z,  \qquad (3)$$

where $z$ is the height of the measurements in meters. Here, we relate the transfer coefficient to the bulk Richardson number, $Rb$ instead of $z/L$ to avoid self correlation. The transfer coefficient can be approximated as a linear function of stability for near neutral conditions [*Louis*, 1979, equation (14)] as

$$C_h = C_{ho}(1 - ARb),  \qquad (4)$$

where $C_{ho}$ is the neutral limit of $C_h$, considered to be a function of the surface roughness and $A$ is a nondimensional coefficient. The surface bulk Richardson number is defined as

$$Rb = \frac{g}{\Theta} \frac{z\Delta T}{V^2}.  \qquad (5)$$

The influence of moisture on the stability can be easily included, but is neglected for the following simple analysis. Based on the original *Louis* [1979] formulation, approximated to lowest order in Richardson number, $A = 15$. The linear dependence of the transfer coefficient on stability is a reasonable assumption only if the bulk Richardson number is small compared to unity. However, our intent here is to qualitatively examine the direct and indirect (through stability) dependencies of the heat flux on the air-sea temperature difference rather than provide numerically accurate values.

[9] To focus on the role of surface temperature variations, we temporarily assume horizontally constant wind speed and surface roughness and thus eliminate wind-related non-linearities analyzed by *Mahrt and Sun* [1995], *Esbensen and McPhaden* [1996], and *Levy and Vickers* [1999]. We then write

$$C_h = C_{ho}(1 - b[\Delta T]),  \qquad (6)$$

where

$$b = A \frac{gz}{\Theta V^2}.  \qquad (7)$$

For $z = 30m$ and V = 5 m s$^{-1}$, $\Theta = 285$ K, $b = 0.63$ $K^{-1}$.

[10] Partitioning the flow into the regional average and deviations of the local average from the regional average and using equation (6), the regionally averaged kinematic heat flux estimated from the bulk formula becomes

$$\frac{[w'\theta']}{C_{ho}V} = -[(1 - b([\Delta T] + \Delta T^*))([\Delta T] + \Delta T^*)],  \qquad (8)$$

where * again indicates deviations of the local average from the regional average. Noting that the regional average of * quantities is zero, equation (8) becomes

$$[w'\theta'] = [w'\theta']_{hom} + bC_{ho}V[(\Delta T)^{*2}],  \qquad (9)$$

where the heat flux for homogenous conditions is

$$[w'\theta']_{hom} = -C_{ho}V(1 - b[\Delta T])[\Delta T].  \qquad (10)$$

The heterogeneity contribution (second term on the right-hand side of equation (9)) is positive, which increases the upward heat flux for unstable conditions, but decreases the downward heat flux for stable conditions. Variations in $\Delta T^*$ occur explicitly through the air-surface temperature difference in the bulk formula, and additionally occur implicitly in the stability function. These two influences work in concert to enhance the flux for unstable conditions. That is, the transfer coefficient is greater in regions of greater unstable air-surface temperature difference. For stable conditions, the explicit influence of $\Delta T^*$ and the implicit influence through $C_h$ oppose each other such that the transfer coefficient is less in regions of greater air-surface temperature difference, thus reducing the spatially averaged flux magnitude. With a mix of unstable and stable subregions, the surface heterogeneity favors transport in the unstable regions and therefore shifts the heat flux to larger upward values.

**Table 1.** Legs for Flight 3, 22 April 2008[a]

| Leg | Length (km) | Heading (deg) | Height (m) | Speed (m s⁻¹) | Wind Direction (deg) | Direction Range (deg) |
|---|---|---|---|---|---|---|
| 1 | 36 | 282 | 336 | 6.2 | 287 | 16 |
| 2 | 33 | 244 | 341 | 4.7 | 272 | 51 |
| 3 | 30 | 328 | 339 | 6 | 238 | 29 |
| 4 | 47 | 159 | 340 | 6.2 | 247 | 30 |
| 5 | 41 | 58 | 342 | 6.4 | 260 | 46 |
| 6 | 56 | 245 | 342 | 5.7 | 272 | 35 |
| 7 | 40 | 325 | 339 | 4.7 | 243 | 37 |
| 8 | 42 | 158 | 337 | 4.8 | 246 | 23 |
| 9 | 39 | 57 | 340 | 4.5 | 267 | 28 |
| 10 | 50 | 245 | 859 | 6.6 | 276 | 50 |
| 11 | 35 | 325 | 27 | 5.6 | 166 | 13 |
| 12 | 48 | 151 | 27 | 5 | 172 | 23 |
| 13 | 46 | 63 | 28 | 4.9 | 189 | 48 |
| 14 | 38 | 234 | 29 | 3.9 | 190 | 49 |
| 15 | 68 | 330 | 30 | 5.8 | 168 | 14 |
| 16 | 84 | 155 | 32 | 5.8 | 173 | 25 |

[a]Leg number, track length (km), aircraft heading (deg), height above the sea surface (m), vector-averaged speed (m s⁻¹), wind direction (deg), and the range of wind direction along the track.

[11] The ratio of the area-averaged heterogeneous contribution to the homogeneous contribution is

$$r = \frac{b[(\Delta T)^{*2}]}{-(1 - b[\Delta T])[\Delta T]}. \quad (11)$$

Note that from equation (7), $b[\Delta T]$ is proportional to the bulk Richardson number. For large $|b\Delta T|$, the linear approximation based on equation (4) is not applicable. For $|b\Delta T|$ small compared to unity, the ratio becomes

$$r \approx \frac{-b[(\Delta T)^{*2}]}{[\Delta T]}. \quad (12)$$

If the air-sea temperature difference is stable (positive $\Delta T$), then the homogeneous and heterogeneous contributions are of opposite sign and equation (12) is negative while the two contributions reinforce each for unstable conditions (equation (12) is positive). Equation (12) indicates that the relative importance of the influence of surface temperature variability on the heat flux is proportional to its variance and inversely related to the strength of the mean air-surface temperature difference. Since $b$ is inverse quadratically related to the wind speed, the surface heterogeneity is more effective in weak wind conditions. With weak winds, small changes in air-surface temperature difference lead to large changes in stability and heat transfer. If the magnitude of $r$ is greater than unity and the homogeneous heat flux is downward, the heterogeneity term could reverse the sign of the area-averaged heat flux; that is, cause counter-gradient regionally averaged upward heat flux.

[12] The above analysis is only a plausibility exercise and neglects the feedback of the surface temperature variation on the momentum flux and wave state and return feedback on $C_h$. The return feedback is due to the relation of $C_h$ to the square root of the stability-dependent drag coefficient or to the momentum roughness length, depending of the form of the similarity theory. *Gulev* [1997] also shows that the correlation between the transfer coefficient and stability can depend significantly on the choice of stability function. We now consider the difficult task of evaluating the total heat flux from aircraft data over a heterogeneous sea surface.

## 3. Data Set

[13] The data were obtained by the Center for Interdisciplinary Remotely-Piloted Aircraft Studies (CIRPAS) Twin Otter aircraft off of the California central coast in April 2008. The instrumentation is described by *Khelif et al.* [2005] with additional details reported by *Khelif et al.* [1999]. The surface temperature was measured by a downward looking Heiman KT 19.85 IR sensor.

[14] To examine the influence of SST variability and the impact of the flux computation method, this study emphasizes Flight 3 conducted on 22 April 2008 deployed off of Monterey Bay, California, USA. Six legs were flown at approximately 30 m above the sea surface with 10 legs flown at higher levels (Table 1). The air-sea temperature difference varied along the track, usually by about 1 K or less. Skies were clear on 22 April.

[15] In general, the surface drag coefficient is small on this day in association with dominant wave heights of only 0.75 m, as indicated by the Scripps wave buoy 46042 at the outer edge of Monterey Bay. The wave direction is 200 degrees, while the surface wind direction is typically between 165 and 190 degrees in the lowest 30 m. The small wave height and modest 30 m winds of roughly 5 m s⁻¹ lead to weak surface stress. As a result, the small horizontal variations of surface temperature and surface heat flux lead to significant variation of stability and turbulence.

[16] Above the surface layer of mostly unstable conditions, the aircraft soundings indicate a slightly stratified (0.5 K/100 m) mixed layer up to about 100 m, with a layer of greater stability (1.0 K/100 m) between 100 and 300 m. In the 100–300 m layer of significant stability, the wind direction rotates from southerly at the bottom of the layer to westerly at the top of the layer. Our analysis will initially concentrate on leg 13 and then considers the other flight legs. Leg 13 is central to the low-level flight period and has a mini warm pool in the center
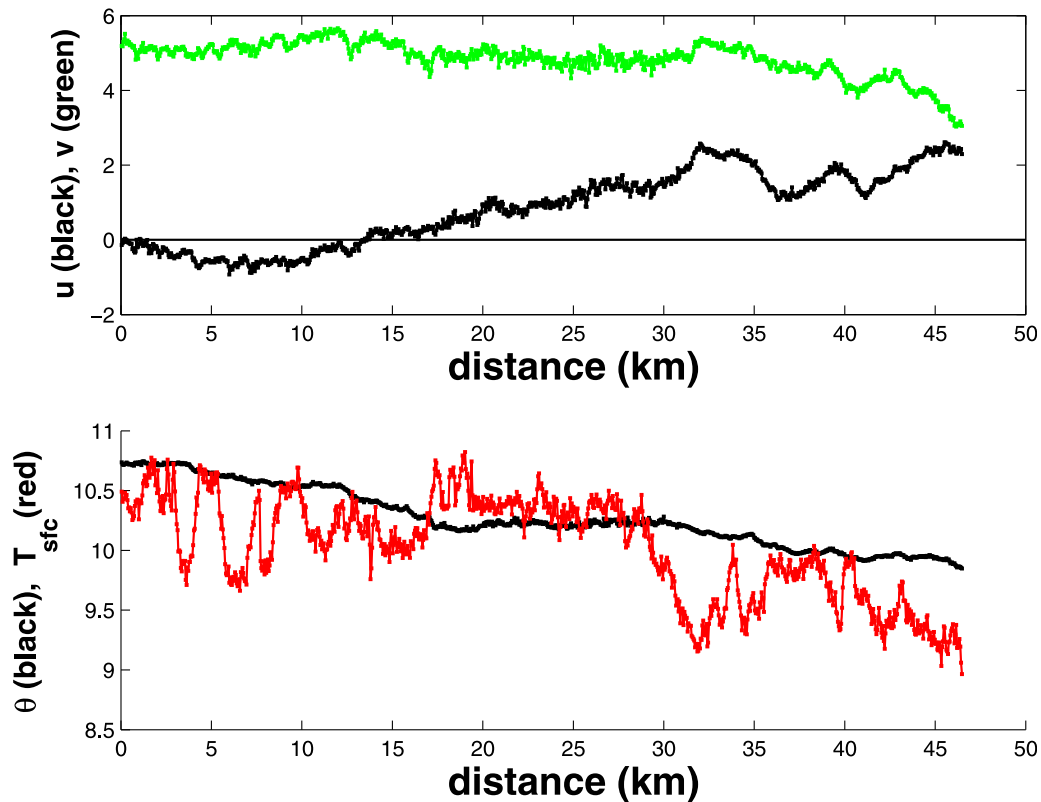
**Figure 1.** Spatial variation of the (top) wind components and (bottom) flight level potential temperature (equation (3)) and surface temperatures for leg 13. The component of the flow in the flight direction is from left to right.

of the track (Figure 1). Three different tracks were used during the flight.

## 4. Flux Analysis

### 4.1. Special Heterogeneity Problems

[17] Estimation of observed heat fluxes over heterogeneous sea-surface temperature incurs several uncertainties.

[18] 1. Meaningful heat fluxes must be averaged over scales much larger than the scale of the main transporting eddies. As a result, the impact of the smallest-scale heterogeneity is not resolved. The averaging over subsegments (local average) still includes heterogeneity within the segment, which might shift the relationship between the heat flux and the air-sea temperature difference compared to the homogeneous case, as illustrated in section 2.

[19] 2. The surface region of influence on the aircraft-measured flux (surface flux footprint) will generally be much larger than the footprint of the downward looking radiometer for measuring the surface temperature, and the footprints may not even overlap with significant wind perpendicular to the track.

[20] 3. Since the range of turbulence scales dominating the flux varies along the flight track, traditional flux calculation methods may not be appropriate and, therefore, a scale-dependent method may be required (next section).

[21] 4. Errors in the measured SST may have a strong impact on the estimated transfer coefficient for heat in cases of small air-sea temperature difference.

[22] 5. The concept and mathematical formalism of an ensemble and standard error do not apply to heterogeneous records.

[23] 6. Over the cooler water, the aircraft level could be too high to estimate the surface flux due to flux divergence between the measurement level and the surface. Horizontal variations of SST may induce important variations of the boundary layer depth, and thus horizontal variations of the flux divergence between the surface and the observational level [*Fairall et al.*, 2006].

[24] We now concentrate on the critical problem of choosing the range of scales included in the perturbation flow over a heterogeneous surface, used to compute fluxes.

### 4.2. Decomposition and Reconstruction

[25] Determination of the "appropriate scales" included in the flux computation becomes problematic with weak turbulence where it may be difficult to separate the turbulence signal from stronger mesoscale motions, as occurs in our case study below. Choice of scales is also problematic with horizontally heterogeneous turbulence where the range of turbulence scales varies horizontally. The spatial variation of the flux at different scales can be examined in terms of a local (wavelet) basis set where the coefficients of the decomposition are studied as a function of horizontal distance. The gain of spatial variation is at the expense of cruder scale resolution compared to Fourier spectra. We do not offer the following technique as a routine procedure for flux calculations, but rather as an analysis tool. Previous applications of wavelet

decomposition to analyze fluxes from aircraft data include *Strunin and Hiyama* [2005] and *Mauder et al.* [2007].

[26] A given variable, $\phi$, at location $x$, can be decomposed as

$$\phi(x) = \sum_{m=1}^{M} A(x, m)\psi_m(x, m) \equiv \sum_{m=1}^{M} \phi'(x, m) \qquad (13)$$

where $A(x, m)$ is the coefficient for the $m^{th}$ (wavelet) basis function at point $x$ and $\psi_m(x, m)$ is the value of the $m^{th}$ wavelet basis function at point $x$ [e.g., *Mallat*, 1989; *Chui*, 1992]. $\phi'(x, m)$ is the $m^{th}$ component of $\phi(x)$. The above shorthand notation ignores the fact that $\psi_m$ is formally defined in terms of the relative position within the wavelet window, but takes advantage of the fact that the wavelet basis for a given scale has one unique value for each point in the record. The scale of the basis functions, $L_m = 2^{m-1} points$, increases dyadically. To facilitate the decomposition, we generate new records with $2^n$ points by interpolating the data to a finer grid. That is, the number of points in the original record is between $2^{n-1}$ and $2^n$, where $n$ depends on the length of the flight leg.

[28] In casual comparisons, we have found the choice of the specific wavelet basis set to be relatively unimportant. We choose the multiresolution basis set with unweighted averaging [e.g., *Howell and Mahrt*, 1997; *Hiscox et al.*, 2006; *Viana et al.*, 2009], which consists of a dyadic set of horizontal straight lines. The multiresolution basis set was recently used to decompose aircraft data in the work of *van den Kroonenberg and Bange* [2007]. This is the only basis set that formally satisfies simple Reynolds averaging. However, this theoretical advantage leads to more fragmented looking phase plots (as in Figure 3). Smoother phase plots can be produced by: (1) using a smoother basis set, (2) using a nonorthogonal decomposition with more scales and renormalizing, or (3) directly smoothing the phase plot. All three methods violate simple Reynolds averaging, and thus do not correspond to the usual budget equations, but may help view the general variability of the flux at different scales. Here, we retain the raw multiresolution decomposition.

[29] One of the deficiencies of previous approaches for computing turbulence quantities is that the larger scales included in the computation are associated with a smaller sample size and greater sampling error, which creates an artificial contribution to the scale dependence of the flux characteristics. To reduce this artificial scale dependence, we define a flux-averaging width, $\tau_F$, that increases with increasing scale $m$, such that the sample size is independent of scale. We write

$$\tau_F(m) \equiv N_F L_m(m) = N_F 2^{m-1} \qquad (14)$$

where the constant, $N_F$, is the specified number of samples for the flux calculation and $L_m$ is the width of the $m^{th}$ wavelet in number of points. With this approach, the flux values for the different scales are computed with the same number of samples, $N_F$, with the limitation that the record length still determines the largest scale that can be adequately sampled. Choice of smaller $\tau_F$ (smaller $N_F$) focuses on finer-scale horizontal structure, at the cost of greater uncertainty. Larger $\tau_F$ provides statistics with a more significant sample size, but coarser spatial resolution (defocusing).

[30] Estimates of the number of samples required to adequately reduce the flux sampling error [*Lenschow et al.*, 1994;

*Mahrt*, 1998] are based on stationary homogeneous conditions. We will nominally choose $N_F = 32$. The qualitative results of this study are not sensitive to the choice of $N_F$.

[31] The flux, $F_{w\phi}$, for a given scale $m$ at point $x_k$ is then

$$F_{w\phi}(m, x_k) = \overline{w'(m, x', x_k)\phi'(m, x', x_k)} \qquad (15)$$

where $x_k$ refers to the central position of the $k^{th}$ flux window for scale $m$ and $x'$ is the relative position within the flux window with respect to $x_k$, the overbar averages over the $N_F$ values of $x'$ within the flux window and $w'$ and $\phi'$ refer to deviations of the flow for the $m^{th}$ scale from the flux window mean. This procedure (equation (15)) generates a new time series of fluxes for each scale. For wavelet decompositions, the scale resolution is only dyadic; that is each scale increases by a factor of two from the previous scale. Greater scale resolution can be obtained in terms of a nonorthogonal decomposition with an arbitrary number of scales. The nonorthogonal decomposition is renormalized to conserve total variance. Here, we employ only the orthogonal decomposition.

## 5. Observed Spatial Structure

### 5.1. Scale-Distance Decomposition

[32] As an example of the kinematic heat flux decomposition based on equation (15), Figure 2 shows $F_{w\theta}(m, x)$ for three different wavelet modes for leg 13. At the scale of maximum heat flux (Figure 2, 22 m, red line), the upward heat flux is concentrated in the zone of positive sea-air temperature difference (Figure 1) in the center of the track. This upward heat flux is due to a combination of decreasing air temperature along the track and a subregion of slightly warmer sea-surface temperature, about +0.5 C warmer than the surrounding water, located between about 17 and 28 km along the track. This small increase of temperature is able to trigger a weak local convective boundary layer. The total turbulent kinematic heat flux in this region is about $10^{-3}$ K m s$^{-1}$. Although small, the surface stress is also small and this heat flux leads to $-z/L > 1$ over the warmer SST region. For lack of a better term, we will refer to this 10 km region as a "mini warm pool." The smaller-scale flux (Figure 2, blue) is more random while the larger-scale flux (Figure 2, green) tends to be downward outside of the mini warm pool.

[33] A more complete dependence on scale is provided by the full wavelet phase plot (Figure 3) where the flux is shown in terms of horizontal scale (y axis) and distance along the flight track (x axis). This phase plot (Figure 3) reveals the dominance of the heat flux by a relatively narrow range of scales centered at 22 m scale over the central mini warm pool. Weaker events of shorter duration generally correspond to the smaller 11 m scale while the strongest upward heat flux event extends to the 44 m scale. At still larger scales, the heat flux tends to be downward, particularly away from the central mini warm pool. Since the flux values for each scale are averaged over the same number of samples (32), the greater "true" variability of the fluxes at the smaller scales is revealed by Figure 3.

### 5.2. Scale Dependence

[34] The heat flux cospectra, scaled by the total heat flux, peaks at a horizontal scale of 22 m (Figure 4, red). The vertical velocity variance (cyan) shows a weak peak at a few meters,
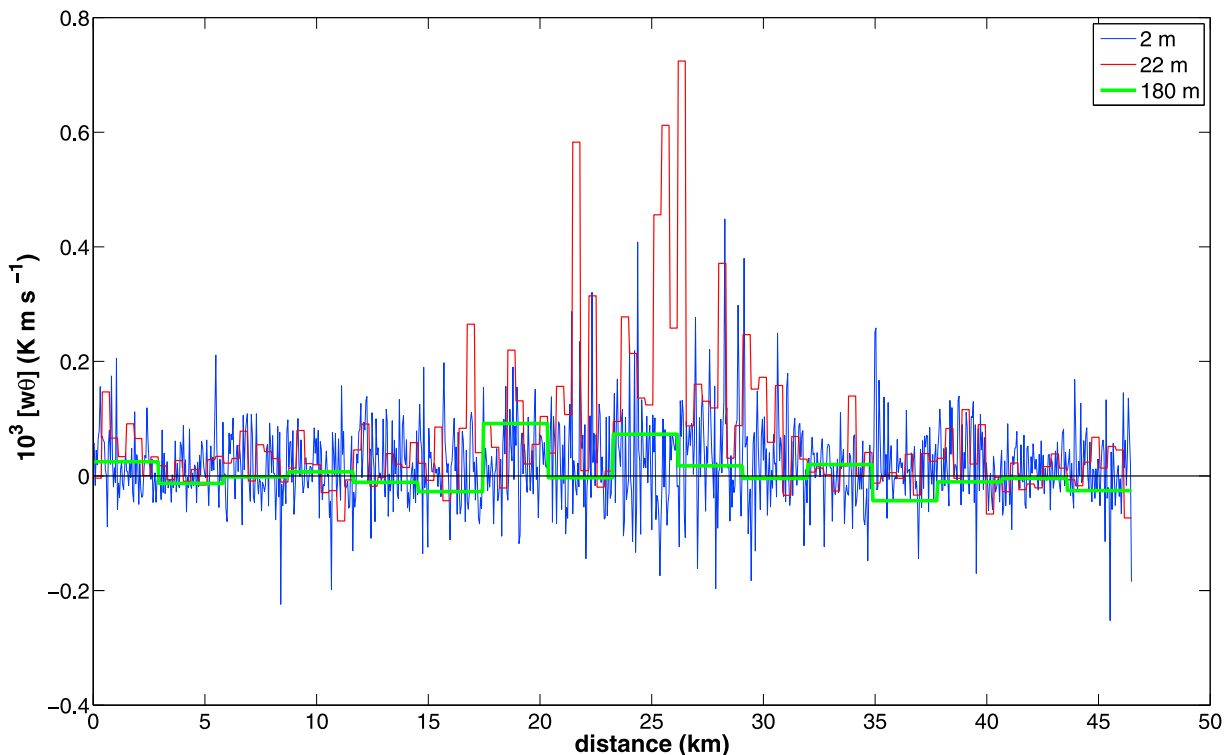
**Figure 2.** Horizontal variation of the kinematic heat flux for three selected modes: the mode of maximum heat flux (22 m, red), a small-scale mode (2 m, blue), and a larger-scale mode (180 m, green).

presumably corresponding to shear-driven turbulence, and then only slowly decreases with increasing scale. The weak turbulent vertical velocities are not large compared to the mesoscale vertical velocities. An inertial subrange in the vertical velocity variance is not observed on this day, nor is it observed in terms of traditional Fourier spectra (not shown), perhaps because the inertial subrange is not resolved by the horizontal resolution, or the constantly changing stability prevents an inertial subrange in terms of the leg-averaged quantities. In fact, Figure 4 suggests that a small amount of heat flux is not resolved by the horizontal resolution of the data, in that the heat flux does not vanish at the smallest scale (left-hand side).

[35] However, bigger uncertainties involve where to truncate the heat flux at the larger-scale end when integrating the cospectra to obtain the turbulent flux. For more strongly convective conditions, the cospectra are better defined and the turbulence flux may dwarf any mesoscale flux [*Lenschow and Sun*, 2007]. However, for the present case of weak heterogeneous flux, more extensive analysis is required.

[36] In particular, the 90 m and 180 m scales are associated with weak upward heat flux, but are actually weak downward outside of the mini warm pool (Figure 3). Should these scales be included as part of the turbulent flux? Should even larger scales be included? The downward heat flux at the 90 m and 180 m scales outside of the warm pool is consistent with larger vertical scales at larger horizontal scales that mix into significant stratification above the 30 m flight level. The heat flux computed from the flight legs at the 300 m level is generally downward, consistent with the stable stratification at this level. However, the fluxes are more erratic at the 300 m

level, compared to the surface, and do not show a well defined relationship to the surface temperature field. This might be partly due to the larger flux footprint at 300 m, compared to near the surface, which might include mostly surface area displaced from the aircraft track due to the cross-track flow.

[37] The 30 m heat flux at the 360 m horizontal scale is large downward, and if included, would seriously reduce the leg averaged upward heat flux. The heat flux values for scales larger than the scale range included in Figure 4 are even of larger magnitude and of either sign. Inclusion of any of these scales substantially changes the total flux and can change the sign. Several of these erratic scales would be included in the "turbulent" flux based on the common practice of computing the fluctuations as deviations from the 1 or 2 km means or even flight-leg means. The selection of scales included in the flux computation is critical for weak turbulence.

[38] We therefore seek more evidence for the selection of scales. The scale dependence of four additional quantities will be examined. The linear correlation coefficient between vertical velocity and temperature fluctuations $Cor_{wT}$ for leg 13 depends on horizontal scale in a manner similar to that for the heat flux (Figure 5) and is relatively small, partly because it reverses sign at several locations along the track. The velocity aspect ratio (anisotropy) is computed for each scale as

$$VAR(m) \equiv \frac{\sqrt{2}[w'w']}{([u'u']^2 + [v'v']^2)^{0.5}} \qquad (16)$$

where the brackets again correspond to averaging over the aircraft leg and all quantities on the right-hand side refer to
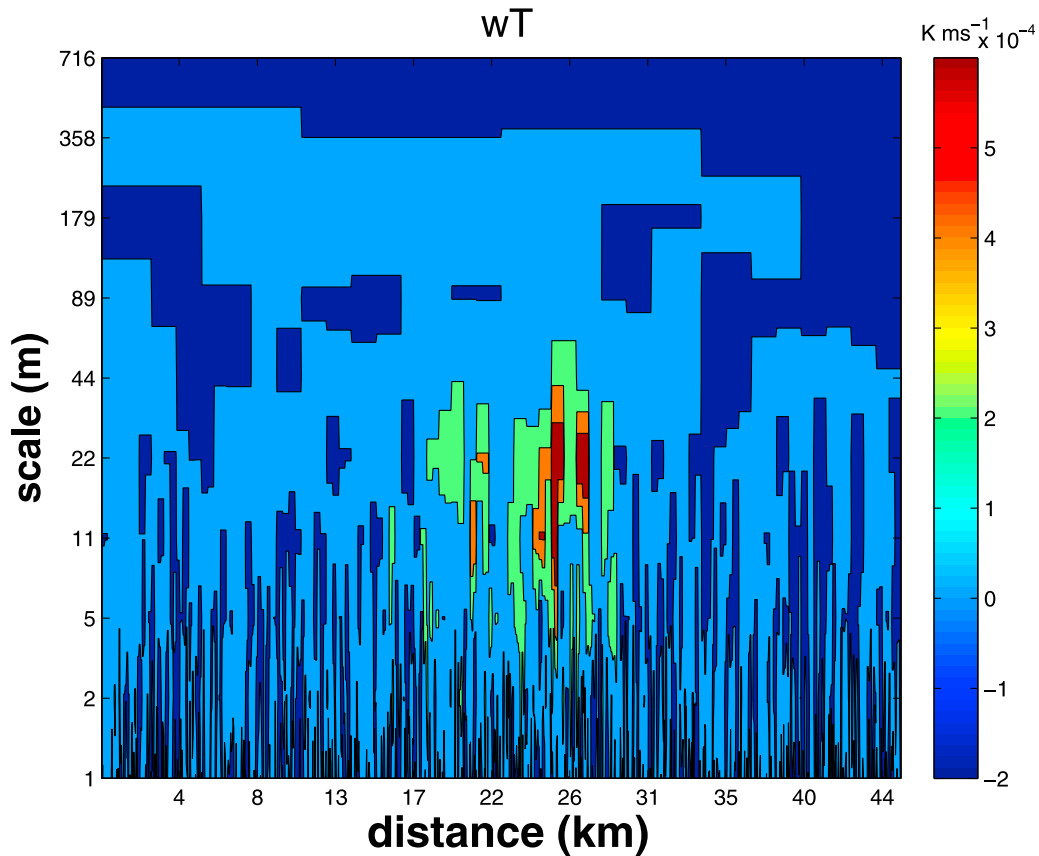
**Figure 3.** Horizontal scale-distance phase plot. Green, orange, and red correspond to increasingly larger upward kinematic heat flux (though still modest), while dark blue corresponds to downward heat flux, as quantified by the color bar. The contours are based on vertical interpolation between the scales.

scale $m$. The multiplication by $\sqrt{2}$ in the numerator leads to $VAR = 1$ when all three variances are equal. For leg 13, the velocity aspect ratio decreases from about 0.7 at the smallest scale to about 0.4 at 180 m. The velocity aspect ratio then decreases abruptly to about 0.1 at the next largest scale (360 m). This appears to be a scale transition region.

[39] A third indicator is constructed by noting that the mesoscale motions near the surface are characterized by weaker vertical velocity fluctuations but larger temperature fluctuations, compared to the turbulence. We therefore compute for each horizontal scale, a nondimensional vertical velocity variance

$$R(m) \equiv \frac{\sqrt{2}[\theta][w'w']}{[T'T']^{0.5}gz} \qquad (17)$$

where all quantities on the right-hand side refer to scale $m$. Specific derivations of $R$ can be formulated in terms of parcel theory by relating $T'$ to $w'$ in terms of the stable stratification, or, relating $w'$ to $T'$ for convective conditions (see references in the work of *Mahrt* [1979]), but here we consider equation (17) to be simply a nondimensional quantity based on the dimensional grounds. On the scale of the main transporting eddies, temperature fluctuations are generated by the eddies acting upon the basic state stratification for stable conditions, while positive temperature fluctuations generate updrafts for unstable stratification. Such derivations are dif-

ficult to apply to the present track where the stability reverses sign along the track.

[40] In order to bound $R$ by unity, we divide $R$ for each scale by the maximum value over all of the scales. This ratio decreases gradually with increasing scale up to 180 m and then decreases more dramatically between 180 m and 360 m (Figure 5). For scales of 360 m and greater, the vertical velocity fluctuations are more constrained by the influence of the surface and the temperature fluctuations are produced by horizontal advection by the mesoscale flow in addition to generation by vertical motions. The 180–360 m scale transition for $R$ is the same as that suggested by $VAR$.

[41] As a fourth characteristic, we define the variation of the flux between flux windows for each scale

$$RFV(m) \equiv \frac{\sigma_{F(m)}}{[abs(F(m))]\sqrt{n}} \qquad (18)$$

where $F(m)$ is the flux for a given flux window, $[F(m)]$ is the average over the entire track and $n$ is the number of flux windows along the track. $RFV(m)$ is mathematically identical to the random flux error, except that the concept of a random error about an ensemble average would apply only to a homogenous record. Although the values of $RFV$ increase with scale for scales greater than the scale of maximum heat flux (not shown), $RFV$ remains small compared to unity for the scales of upward transport. $RFV$ becomes order of unity
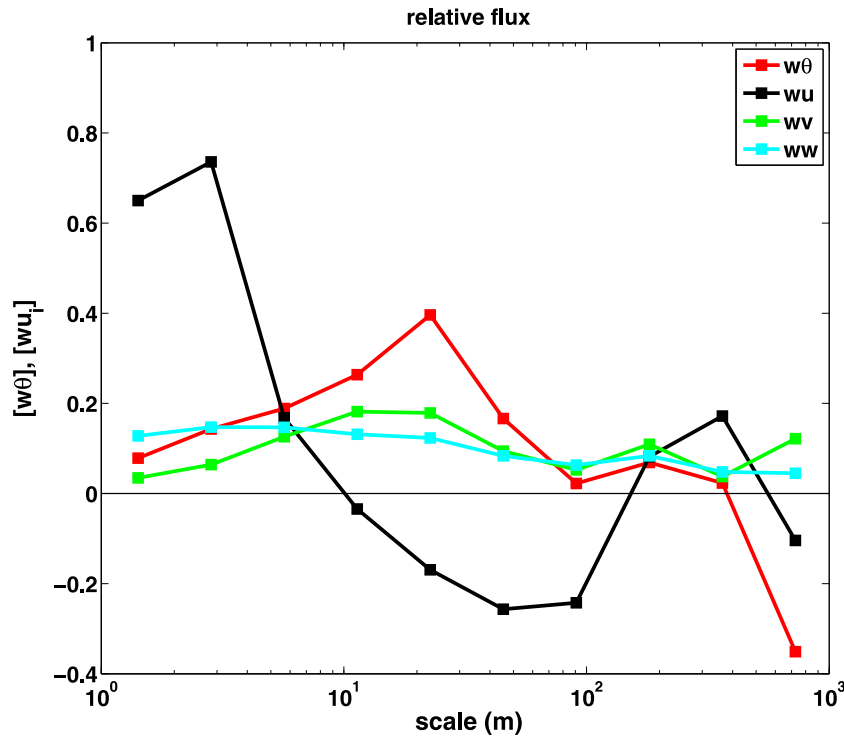
**Figure 4.** The flux cospectra for a given scale, normalized by the total kinematic flux integrated over all of the scales, as a function of scale.

for the 90–180 m scales and then becomes much larger for scales of 360 m and greater. *RFV* and the variation of the flux between flux windows is partly due to the large skewness of the window heat flux, as shown in Figure 6 for the scale of maximum heat flux (22 m). The few large values that dominate the leg-averaged flux are associated flux events over the mini warm pool.

[42] The above four indicators for leg 13 collectively suggest that the 90 m and 180 m scales should be included in the turbulent heat flux, but scales of 360 m and larger should not be included. Therefore, a horizontal truncation scale, $L_{trun}$, is determined as the largest scale included as turbulence and is chosen to be the 180 m mode for the current flight leg. Similar conclusions are reached for the other legs (Tables 1 and 2) although the behavior of the four indicators varies enough between legs to discourage construction of an automated method for determination of $L_{trun}$. The choice of $L_{trun}$ is least conclusive for the two shortest legs (11 and 14). $L_{trun}$ varies significantly between legs, as discussed in the next section.

## 6. Integration and Spatial Variation of Fluxes

[43] The turbulent fluxes are computed by integrating the flux cospectra over the selected range of horizontal scales up to the selected largest scale, $L_{trun}$. To compute the flux for each data point, the flux for each scale (equation (15)) is projected onto each point and then the fluxes are summed over all of the scales up to $L_{trun}$ at each point. The integrated flux at point $x$ is then

$$\sum_{m=1}^{N_{trun}} F_{w\phi}(m,x) \qquad (19)$$

where $N_{trun}$ is the mode number of the largest scale included in the flux calculation, which corresponds to $L_m = 180$ m for leg 13.

[44] The turbulent heat flux from equation (19) responds to SST variations mainly on scales greater than a few kilometers for the present data. For display in Figure 7, the fluxes computed from equation (19) are averaged arbitrarily over $L_{ave} = 2.9$ km for leg 13, producing 16 flux averages along the flight path. To summarize, our analysis has been based on the choice of: (1) $L_{trun}$ to define the largest scale included as
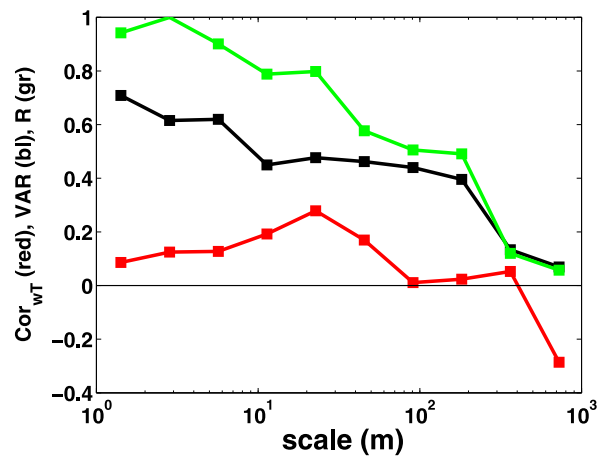


**Figure 5.** The velocity aspect ratio (black), correlation between temperature and vertical velocity (red), and scaled vertical velocity variance, $R$ (green), as a function of scale (m).
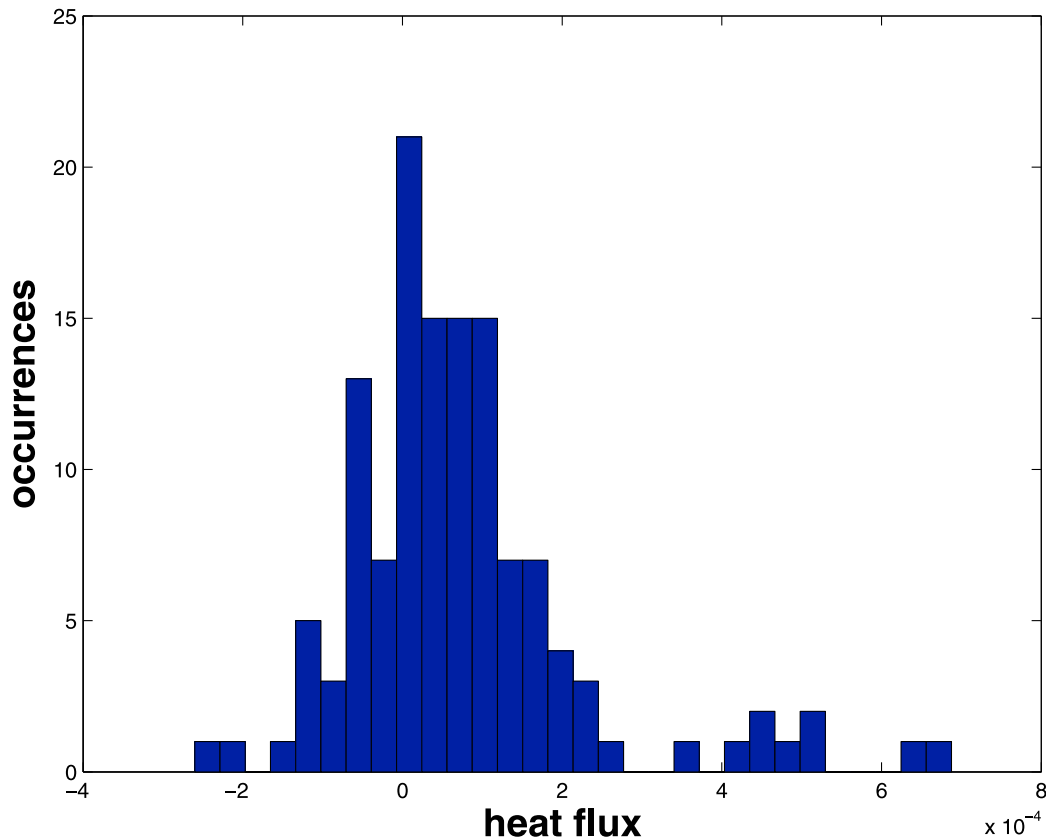
**Figure 6.** The frequency distribution of the window kinematic heat flux (K m s$^{-1}$) for the scale of maximum upward heat flux for leg 13.

turbulence, (2) the flux averaging width ($N_F L_m = 32 L_m$), and (3) the additional averaging over $L_{ave}$ for display in Figure 7.

[45] For comparison, we also choose a more strongly truncated calculation extending up to only the 45 m scale (Figure 7, green line). The main impact is the expected increase of upward heat flux outside of the mini warm pool. In fact, the extremely weak integrated downward heat flux at the northeast end of the flight track changes to weak upward heat flux. However, this more severe truncation does not seriously change the leg-averaged heat flux, which remains dominated by the mini warm pool.

[46] The use of a position-dependent $N_{trun} = f(x)$, constructed by applying the analysis of section 5.2 to different segments of the track, reduces the magnitude of the downward heat flux outside of the warm pool and again reverses some very small downward values to upward heat flux. However, $N_{trun} = f(x)$ only slightly increases the track-averaged

upward heat flux because of the dominance of the central mini warm pool. Therefore, for this flight leg, the main use of the multiresolution decomposition and attendant scale-dependent indices (section 5.2) is to more intelligently choose the constant truncation scale for the flight leg rather than a variable truncation scale. The choice of a position-dependent truncation scale would presumably be more important for larger variations of SST compared to the present case study. Observational difficulties (section 4.1) probably also play an important role. While Figure 7 shows that the leg-averaged flux is not sensitive to the precise choice of scales for this particular leg, inclusion of scales greater than 360 m leads to erratic behavior of the flux.

### 6.1. Moisture Flux

[47] The moisture flux contributes significantly to the leg-averaged virtual heat flux, partly because the heat flux is

**Table 2.** Turbulent Statistics for the Six Low-Level Legs on Flight 3, 22 April[a]

| Leg | wT × 10$^3$ (K m s$^{-1}$) | $z/L$ | Maximum wT (m) | $R$ (m) | $r_{wT}$ | Maximum Down (m) | $L_{trun}$ (m) |
|-----|------|-------|-------|-----|------|-------|------|
| 11 | 0.39 | −0.17 | ** | 30 | 0.05 | 100 | 140 |
| 12 | 0.19 | −0.15 | 12 | 35 | 0.15 | 300 | 380 |
| 13 | 0.30 | −0.88 | 20 | 70 | 0.20 | 140 | 180 |
| 14 | 0.44 | −0.41 | 13 | 30 | 0.21 | 250 | 300 |
| 15 | 0.45 | −0.24 | 34 | 40 | 0.19 | 300 | 535 |
| 16 | 0.50 | −0.15 | 18 | 20 | 0.13 | 500 | 660 |

[a]Leg number, total integrated heat flux (10$^{-3}$ K m s$^{-1}$), $z/L$ based on the virtual heat flux, the scale of maximum heat flux (m) using scale interpolation, $R$, the correlation between $\theta'$ and $w'$ at the scale of maximum heat flux ($r_{wT}$), the scale of maximum downward heat flux (m) using scale interpolation, and $L_{trun}$, the maximum scale included in the flux calculations (m). ** indicates that the cospectral maxima was too ambiguous to determine a numerical value.
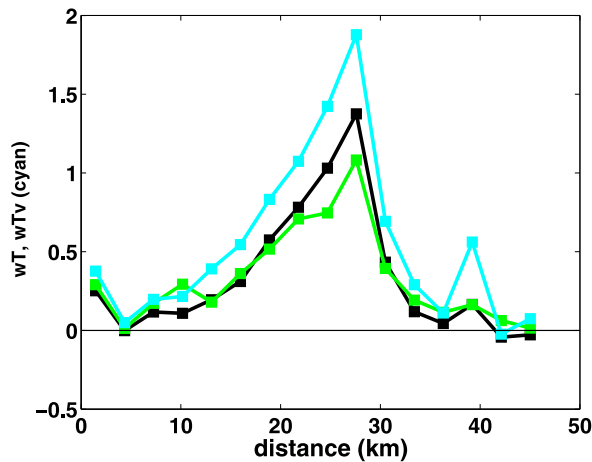
**Figure 7.** The integrated kinematic heat flux ($10^{-3}$ K m s$^{-1}$) through the 180 m mode (black line), through the 45 m mode (green line), and the kinematic virtual heat flux integrated through the 180 m mode (cyan line), as a function of horizontal distance for leg 13.

small and sometimes reverses sign while the moisture flux is always upward. As a result, the correlation between the vertical velocity fluctuations and the moisture fluctuations is greater than the correlation between the vertical velocity fluctuations and temperature fluctuations. For leg 13, the upward moisture flux causes the virtual heat flux to be upward for two of the three segments where the heat flux is slightly downward (Figure 7, cyan). Future studies will require the choice between computing $L_{trun}$ separately for moisture and temperature or choosing a single value based on joint analysis of temperature and moisture.

### 6.2. Other Legs

[48] The above indices (section 5.2) were also applied to the other low-level flight legs to select the maximum scale (truncation scale) in the integrated flux calculation (Table 2). For perspective, leg 13 has the highest value of $-z/L$ based on the leg-averaged momentum fluxes and virtual heat flux, mainly due to small values of the momentum flux. The truncation scale, $L_{trun}$, varies substantially between legs, which appears to be partly due to the orientation of the track with respect to the mean wind direction and possible elongation of eddies in the wind direction [*Lenschow*, 1970]. There is no obvious relation of $L_{trun}$ to stability for the present heterogenous data. The very weak fluxes are probably significantly nonstationary. Only a large number of repeated passes over the same track can address this issue.

[49] The transfer coefficient for the bulk formula was evaluated for each leg based on leg-averaged quantities. Four of the six legs were characterized by counter gradient fluxes (negative transfer coefficient). Unstable parts of the leg dominated the leg-averaged heat flux while the leg-averaged air-sea temperature differences were dominated by the broader regions of weakly stable conditions. However, the values of the transfer coefficients and relation to stability were sensitive to the calibration of the SST. As a result, for the small leg-averaged air-sea differences, quantitative evaluation of the behavior of the transfer coefficient is too uncertain. For some of the legs, the transfer coefficient for the spatially

averaged flux varies significantly with even small changes of only 0.1 K in the calibration. As an additional complication, the aircraft flight level of 30 m may be too high for estimation of the air-sea temperature difference in the bulk formula for subregions of stable stratification and very weak turbulence where the surface layer may be much thinner than 30 m.

### 6.3. Other Flights

[50] Brief analysis of other flights from the same field program revealed that the calculation of the fluxes for flights with stronger turbulence are less sensitive to the flux calculation method and the exact value of the SST. In contrast, with weak turbulence, the turbulence vertical velocities are no longer large compared to mesoscale vertical velocities. Then, separation of turbulence from mesoscale motions becomes more difficult and more important and traditional methods may inadvertently include erratic mesoscale fluxes in the computation. Unfortunately, universal rules for computing fluxes over heterogeneous surfaces cannot be established.

## 7. Conclusions

[51] This study identifies the potential importance of small variations of the SST for small mean air-sea temperature difference. The horizontal heterogeneity of the SST is predicted to increase the area-averaged heat flux for weakly unstable conditions and decrease the area-averaged downward heat flux for weakly stable conditions. For slightly stable area-averaged air-sea temperature difference, variations of the air-sea temperature difference can even lead to "counter gradient" upward area-averaged heat flux. A simple analytical development indicates that the influence of variation of the air-sea temperature difference on the area-averaged heat flux is proportional to the square of the SST variability and inversely related to the horizontally averaged air-sea temperature difference and the square of the wind speed.

[52] The usual methods of computing fluxes may be inadequate over heterogeneous surfaces. Inadvertent inclusion of larger mesoscale motions leads to erratic fluxes. In this study, fluxes were computed from a decomposition into a local (wavelet) basis set where the coefficients of the expansion are allowed to vary with the heterogeneity. This approach not only provides information on the spatial variability of the contribution of different scales to the total flux, but also provides more information for selecting the range of scales included in the flux calculation. This study used the scale dependence of a number of different flow characteristics to assist in determination of the range of scales included in the turbulent flux calculation. An automated version of the present method for computing fluxes is not obvious.

[53] The case study for small air-sea temperature difference indicates that small variations of the air-sea temperature difference, here on scales of 50 km or less and magnitudes less than 1K, can significantly increase the area-averaged upward surface heat flux beyond the homogenous prediction. Unfortunately, evaluation of the transfer coefficient for the heat flux requires very accurate measurements of SST variation. As a result of the small surface friction velocity for the case study, small variations of the air-sea temperature difference lead to large variation of $z/L$. While small heat fluxes are not significant for some applications, small heat fluxes

may occupy a large fraction of the total oceanic surface and thus play a significant role in the global heat flux budget. More rigorous investigations require a large number of repeated passes along the same low-level track with accurate SST measurements, as well as attention to observational difficulties noted in section 4.1.

# References

Chui, C. K. (1992), *An Introduction to Wavelets*, Academic, Boston.

Esbensen, S., and M. McPhaden (1996). Enhancement of tropical ocean evaporation and sensible heat flux by atmospheric mesoscale systems, *J. Clim.*, 9, 2307–2325, doi:10.1175/1520-0442(1996)009.

Fairall, C. W., L. Bariteau, A. A. Grachev, R. J. Hill, D. E. Wolfe, W. A. Brewer, S. C. Tucker, J. E. Hare, and W. M. Angevine (2006), Turbulent bulk transfer coefficients and ozone deposition velocity in the International Consortium for Atmospheric Research into Transport and Transformation, *J. Geophys. Res.*, 111, D23S20, doi:10.1029/2006JD007597.

Friehe, C. A., W. J. Shaw, D. P. Rogers, K. L. Davidson, W. G. Large, S. A. Stage, G. H. Crescenti, S. J. S. Khalsa, G. K. Greenhut, and F. Li (1991), Air-sea fluxes and surface layer turbulence around a sea-surface temperature front, *J. Geophys. Res.*, 96, 8593–8609.

Grachev, A. A., and C. W. Fairall (2001), Upward momentum transfer in the marine boundary layer, *J. Phys. Oceanogr.*, 31, 1698–1711, doi:10.1175/1520-04852001031.

Grachev, A., C. Fairall, J. Hare, J. Edson, and S. Miller (2003), Wind stress vector over ocean waves, *J. Phys. Oceanogr.*, 33, 2408–2429, doi:10.1175/1520-04852003033.

Gulev, S. (1997), Climatologically significant effects of space-time averaging in the North Atlantic sea-air heat flux fields, *J. Clim.*, 10, 2743–2763, doi:10.1175/1520-0442(1997)010<2743:CSEOST>2.0.CO;2.

Hiscox, A., C. Nappo, and D. Miller (2006), On the use of lidar images of smoke plumes to measure dispersion parameters in the stable boundary layer, *J. Atmos. Oceanic Technol.*, 23, 1150–1154, doi:10.1175/JTECH1896.1.

Howell, J., and L. Mahrt (1997), Multiresolution flux decomposition, *Boundary Layer Meteorol.*, 83, 117–137, doi:10.1023/A:1000210427798.

Katsaros, K. B., and A. V. Soloviev (2004), Vanishing horizontal sea surface temperature gradients at low wind speeds, *Boundary Layer Meteorol.*, 112, 381–396, doi:10.1023/B:BOUN.0000027905.90989.b2.

Katsaros, K. B., A. V. Soloviev, R. H. Weisberg, and M. E. Luther (2005), Reduced horizontal sea surface temperature gradients under conditions of clear skies and weak winds, *Boundary Layer Meterol.*, 116, 175–185.

Khelif, D., C. Friehe, H. Jonsson, Q. Wang, and K. Radosc (2005), Wintertime boundary-layer structure and air-sea interaction over the Japan/East Sea, *Deep Sea Res.*, 52, 1525–1546, doi:10.1016/j.dsr2.2004.04.005.

Khelif, S., S. Burns, and C. Friehe (1999), Improved wind measurements on research aircraft, *J. Atmos. Oceanic Technol.*, 16, 860–875, doi:10.1175/1520-04261999016.

Lenschow, D. (1970), Airplane measurements of planetary boundary layer structure, *J. Appl. Meteorol.*, 9, 874–884, doi:10.1175/1520-0450(1970)009.

Lenschow, D., and J. Sun (2007), The spectral composition of fluxes and variances over land and sea out to the mesoscale, *Boundary Layer Meteorol.*, 125, 63–84, doi:10.1007/s10546-007-9191-8.

Lenschow, D. H., J. Mann, and L. Kristensen (1994), How long is long enough when measuring fluxes and other turbulence statistics, *J. Atmos. Oceanic Technol.*, 11, 661–673, doi:10.1175/1520-0426.

Levy, G., and D. Vickers (1999), Surface fluxes from satellite winds: Modeling air-sea flux enhancement from spatial and temporal observations, *J. Geophys. Res.*, 104, 20,639–20,650.

Louis, J.-F. (1979), A parametric model of vertical eddy fluxes in the atmosphere, *Boundary Layer Meteorol.*, 17, 187–202, doi:10.1007/BF00117978.

Mahrt, L. (1979), Penetrative convection at the top of the growing boundary layer, *Q. J. R. Meteorol. Soc.*, 205, 469–485, doi:10.1002/qj.49710544411.

Mahrt, L. (1998), Flux sampling errors for aircraft and towers, *J. Atmos. Oceanic Technol.*, 15, 416–429.

Mahrt, L., and J. Sun (1995), Dependence of surface exchange coefficients on averaging scale and grid size, *Q. J. R. Meteorol. Soc.*, 121, 1835–1852, doi:10.1002/qj.49710544411.

Mahrt, L., D. Vickers, and E. Moore (2004), Flow adjustments across sea-surface temperature changes, *Boundary Layer Meteorol.*, 111, 553–564, doi:10.1023/B:BOUN.0000016600.63382.5f.

Mallat, S. G. (1989), A theory of multiresolution signal decomposition: The wavelet representation, *IEEE Trans. Pattern Anal. Machine Intell.*, 7, 674–693, doi:10.1109/34.192463.

Mauder, M., R. L. Desjardins, and I. MacPherson (2007), Scale analysis of airborne flux measurements over heterogeneous terrain in a boreal ecosystem, *J. Geophys. Res.*, 112, D13112, doi:10.1029/2006JD008133.

O'Neill, L. W., D. B. Chelton, S. K. Esbensen, and F. J. Wentz (2005), High-resolution satellite measurements of the atmospheric boundary layer response to SST perturbations over the Agulhas Return Current, *J. Clim.*, 18, 2706–2723, doi:10.1175/JCLI3415.1.

Pyatt, H. E., A. Albrecht, C. W. Fairall, J. E. Hare, N. Bond, P. Minnis, and J. K. Ayers (2005), Evolution of marine atmospheric boundary layer structure across the cold tongue-ITCZ complex, *J. Clim.*, 18, 737–753, doi:10.1175/JCLI-3287.1.

Rieder, K. F., and J. A. Smith (1998), Removing wave effects from the wind stress vector, *J. Geophys. Res.*, 103, 1363–1374.

Small, R. J., S. P. deSzoeke, S. P. Xie, L. O'Neil, H. Seo, Q. Song, P. Cornillon, M. Spall, and S. Minobe (2008), Air-sea interaction over ocean fronts and eddies, *Dyn. Atmos. Oceans*, 45, 274–319.

Smedman, A.-S., M. Tjernström, and U. Hogström (1994), The near-neutral marine atmospheric boundary layer with no surface shearing stress: A case study, *J. Atmos. Sci.*, 51, 3399–3411, doi:10.1175/1520-04691994051.

Smedman, A.-S., U. Högström, E. Sahlée, and C. Johansson (2007a), Critical re-evaluation of the bulk transfer coefficient for sensible heat over the ocean during unstable and neutral conditions, *Q. J. R. Meteorol. Soc.*, 133, 227–250.

Smedman, A.-S., U. Högström, J. C. R. Hunt, and E. Sahlée (2007b), Heat/mass transfer in the slightly unstable atmospheric surface layer, *Q. J. R. Meteorol. Soc.*, 133, 37–51, doi:10.1002/qj.7.

Soloviev, A., and R. Lukas (2006), *The Near-Surface Layer of the Ocean: Structure, Dynamics and Applications*, 572 pp., Springer, New York.

Strunin, M. A., and T. Hiyama (2005), Spectral structure of small-scale turbulent and mesoscale fluxes in the atmospheric boundary layer over a thermally inhomogeneous land surface, *Boundary Layer Meteorol.*, 117, 479–510, doi:10.1007/s10546-005-2188-2.

Thum, N., S. K. Esbensen, D. B. Chelton, and M. McPhaden (2002), Air-sea heat exchange along the northern sea surface temperature front in the eastern tropical Pacific, *J. Clim.*, 15, 3361–3378, doi:10.1175/1520-04422002015.

Ullman, D., and P. Cornillon (2000), Evaluation of front detection methods for satellite-derived SST data using in situ observations, *J. Atmos. Oceanic Technol.*, 17, 1667–1675, doi:10.1175/1520-04262000017.

van den Kroonenberg, A., and J. Bange (2007), Turbulent flux calculation in the polar stable boundary layer: Multiresolution flux decomposition and wavelet analysis, *J. Geophys. Res.*, 112, D06112, doi:10.1029/2006JD007819.

Viana, S., C. Yagüe, and G. Maqueda (2009), Propagation and effects of a mesoscale gravity-wave over a weakly-stratified stable boundary layer during SABLES2006 field campaign, *Boundary Layer Meteorol.*, 133, 165–188, doi:10.1007/s10546-009-9420-4.

Vickers, D., and L. Mahrt (2006), Evaluation of the air-sea bulk formula and sea-surface temperature variability, *J. Geophys. Res.*, 111, C05002, doi:10.1029/2005JC003323.

D. Khelif, Department of Mechanical and Aerospace Engineering, University of California, Irvine, CA 92697, USA.

L. Mahrt, COAS, Oregon State University, Corvallis, OR 97331, USA. (mahrt@nwra.com)